Correlations for photocatalytic activity and spectral features of the absorption band edge of TiO₂ modified by thiourea

V. Nadtochenko [a,*], N. Denisov [a], A. Gorenberg [a], Yu. Kozlov [a], P. Chubukov [c], J.A. Rengifo [b], C. Pulgarin [b], J. Kiwi [b]

[a] Institute of Problems of Chemical Physics, Russian Academy of Sciences, Semenov av.1, 142432 Chernogolovka, Russia
[b] Ecole Polythechnique Fédérale de Lausanne (EPFL-SB-ISIC-GGEC). Group of Electrochemical Engineering, Station 6, CH-1015, Switzerland
[c] Moscow Institute of Physics and Technology, Institutskii per. 9, 141700 Dolgoprudny, Moscow Region, Russia

ARTICLE INFO

ABSTRACT

Doping of nanocrystalline TiO₂ powders with sizes ranging from 9.5 nm up to 19.1 nm was carried out with thiourea (TU) to introduce the C, N and S-species into the TiO₂. The crystal size was determined by X-ray diffraction. Doped-TiO₂ particles were colored while the undoped TiO₂ was white. The edge of the absorption band edge was analyzed to describe the TiO₂ band gap according to the indirect transitions theory of semiconductors. In the former analysis the energy distribution of the doped centers is discussed in terms of the Urbach's tail theory ($K = K_0 \exp(\sigma((h\nu - E_g)/kT))$), being K the absorbance in the Kubelka–Munk equation. Evidence is presented for thiourea doped-TiO₂ leading to Urbach's tail associated with the formation of states in the band-gap rather than a narrowing of the band gap. The photocatalytic activity of the doped-TiO₂ was tested by the reduction of tetra-nitromethane to nitroform and by the oxidation of I^- to I_3^-. The rate of formation of nitroform (NF) produced under 460 nm light increased for the smaller TiO₂ nanoparticles. This suggests the formation of localized centers under 460 nm light. But under 366 nm light, the highest rate of NF formation was observed for samples with the biggest nanocrystal size. Under 366 nm light, the smaller particles show a low rate of nitroform formation due to a more favorable band-gap electron-hole recombination. Lipid phosphatidyl-ethanolcholine (PE) under 460 nm visible light in the presence of doped-TiO₂ led to the formation of conjugated of double bonds in PE. This implies the formation of peroxy radicals due to the TiO₂ e^-_{cb} localized electronic states under visible light irradiation.

1. Introduction

TiO₂ with photocatalytic activity in the visible range is a topic of great importance in view of the applications in energy storage and environmental pollution control. The activity under visible light would make possible a wider use of TiO₂. Bulk or surface modifications of TiO₂ doping with carbon [1–5], nitrogen [6–13], and sulfur [14–18] has been reported to induce visible absorption in TiO₂. The dopants generate electronic states close to the valence band edge introducing a visible absorption shoulder between 400 and 600 nm in the TiO₂. The photoactivity of the doped materials has been reported to be lower in the visible than in the UV-region [1–18]. For a more efficient utilization of visible light in photocatalytic processes we modified TiO₂ to shift the absorption into the visible part of the solar spectrum. Asahi et al., introducing

N-atoms to narrow the TiO₂ band gap have reported an increase in absorption in the visible region [1]. Irie et al. argued that the isolated narrow band formed above the valence band was responsible for the response in the visible region [8]. However, Ihara et al. suggest that oxygen vacancies contribute to the absorption in the visible region and that the doped N-atoms only enhance the stabilization of these oxygen vacancies [19]. Visible region photocatalysis involving TiO₂ oxygen vacancies has been recently reported by Martyanov et al., [20]. Serpone suggested that the red shift of the TiO₂ absorption edge was due to the formation of color centers (F-centers) [21].

Previously Bacsa et al. [18] reported doped-TiO₂ by thiourea (TU) leading to the formation of TiO₂ nanoparticles with a core/shell structure where the N, S, and C dopants were localized in the ∼3 nm shell layer. The sputtering with Ar-ions enabled to find the depth profile of the elements in the 20 top-most layers of the S-TiO₂ catalyst and made possible to locate S on the TiO₂ top-most layers [18]. Recently, the TiO₂ core/shell structure has been reported by Kisch et al., for urea doped TiO₂ [22]. In the present

* Corresponding author.
E-mail address: John.Kiwi@epfl.ch (J. Kiwi).

work we investigate the photocatalytic activity of doped-TiO$_2$ samples modified by N, S, and C by adding thiourea. The reduction of tetranitromethane to nitroform and the oxidation of I$^-$ to I$_3^-$ are used as test reactions. The degradation of tetranitromethane by undoped TiO$_2$ during photocatalytic processes has been reported [23]. The present work focuses on how the crystal size of the doped TiO$_2$ particle and the distribution of the energy states in the doped-TiO$_2$ band-gap due to the N, S, and C correlate with the observed photocatalytic activity.

2. Experimental

2.1. TiO$_2$ synthesis

Titanium-tetra-isopropoxide solution Ti(iPrOH)$_4$ (Aldrich) was mixed with acetic acid Ti(iPrOH)$_4$: AcOH = 1:1 (mol). This solution was added dropwise to 0.03 M HNO$_3$ (1:3 volume ratio) under vigorous stirring and cooled externally by ice during the mixing time. The resulting solution was turbid. A quarter of the solution was peptized at 20 °C during 2 days, and later dried at 100 °C. The resulting powder was used as a precursor for the sample #1. The rest of the original solution was gelated at 80 °C during 0.5 h followed by peptization at 20 °C during 2 days. A third of this solution was dried at 100 °C and this powder was used as a precursor for the sample #2. The residual colloid was treated hydrothermally in a Teflon-lined autoclave at 230 °C during 16 h, leading to a sol and a precipitate. The sol and precipitate were separated and dried at 100 °C. Powder from the sol was used as a precursor for the sample #3 and the precipitate used as a precursor for the sample #4. Control experiments were carried out with Degussa TiO$_2$ Aeroxide® P-25.

The different TiO$_2$ powders obtained as described above were mixed with thiourea (Aldrich), grinded and annealed at 500 °C during 3 h. As a control samples of TiO$_2$ (#1b-#4b) were prepared in parallel to samples #1-#4: all prepared powders were annealed at 500 °C during 3 h without mixing with thiourea. The BET measurements were carried out by using an Autosorb-1, Quantachrome Corp., USA.

### 2.2. Optical absorption spectra

UV–vis spectroscopy was carried out with a Cary 51 spectrophotometer. Suspensions were adequately centrifuged before each measurement. The ultraviolet-visible diffuse reflectance spectra of TiO$_2$ powders were measured with a Specord 40 spectrophotometer provided with a diffuse reflectance accessory. The Kubelka–Munk relations measuring K/S for thick samples with low optical transmittance allowed the conversion of the reflectance (R) into the equivalent absorption spectra. K and S are the absorption and scattering coefficients of TiO$_2$. The reflectance of MgO was used as reference (R_{MgO}) [18].

$$R_\infty = \frac{R}{R_{MgO}} \tag{1}$$

$$\frac{K(\lambda)}{S(\lambda)} = \frac{(1 - R_\infty)^2}{2R_\infty} \tag{2}$$

2.3. XRD measurements

The crystalline phase of the TiO$_2$ samples were determined with the help of an ARL X'TRA (Thermo electron corporation). The X-ray diffractometer used the Cu K$_a$-radiation to reference the observed peaks
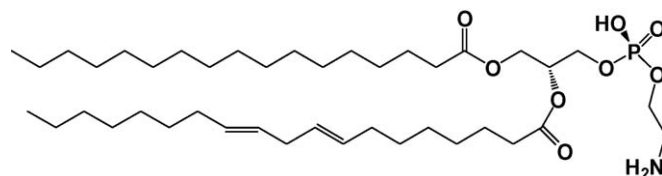
Scheme 1. Chemical structure of L-α-phosphatidyl-ethanolamine (PE).

2.4. Sample preparation for irradiation experiments

L-α-phosphatidyl-ethanolamine (L-α-cephaline)PE from bovine brain (Aldrich, AG Buchs) was used as received. The chemical structure of PE is shown in Scheme 1. PE multi-lamellar vesicles were prepared in following way: first, a thin dry PE film was spread on a glass surface of a beaker. The vesicles were stirred in solution (10 mg/ml), with Raschig glass rings under a vigorous flow of N$_2$ gas. As the reaction time progressed, the PE-lipid film transformed into a multi-lamellar turbid vesicle suspension. This suspension was mixed with TiO$_2$–thiourea and purged with O$_2$ for 3 min.

2.5. Spectrophotometric detection of conjugated dienes

To measure the rate of formation of conjugated dienes, 100 µl of the vesicle suspension was diluted in 1 ml of H$_2$O. The absorption spectra were measured in a quartz cell with an optical pathlength of 0.1 cm. Conjugated dienes show a distinct absorption in the UV at 234 nm for the cis-isomer (28,000 dm^3 mol^{-1} cm^{-1}) and at 236 nm for the trans-isomer (26,000 dm^3 mol^{-1} cm^{-1}). The optical density of the conjugated dienes concentration was monitored at 234 nm.

2.6. Photocatalytic activity measurements

These measurements were carried out with TiO$_2$ concentration of 1 mg/ml in 5 ml Pyrex tubes stirring at room temperature and open to air. Millipore bi-distilled water was used throughout at pH 6. The 4 'TL' 8W/05 Philips lamps emitted light between 300 and 400 nm with a maximum at λ = 365 nm and were used in the UV irradiation experiments. Lamps were equipped in the box 30 × 30 × 60 cm made from Al. Philips lamp light power was 4 mW/cm^2, as measured by a light power meter. The blue photodiode was used for the visible light excitation in the range of 440–480 nm with a maximum at λ = 460 nm having a light flux of 10 mW/cm^2. Isopropanol was used as sacrificial donor during the TiO$_2$ mediated photocatalysis in the concentration of 20%. The concentrations of C(NO$_2$)$_4$ and KI ChimMed® used during the photocatalytic testing were: [C(NO$_2$)$_4$] = 2 × 10^{-4} M and [KI] = 1 M.

3. Results and discussion

3.1. UV–vis diffuse reflection spectroscopy (DRS) of TiO$_2$ powders

Fig. 1 shows the UV–vis spectra of the modified TiO$_2$ powders as described in Section 2.2 of the experimental part. The rough UV–vis reflectance data cannot be used directly to assess the absorption coefficient of the powders because of the large scattering contribution to the reflectance spectra. Normally it is assumed a weak dependence of the scattering coefficient S on the wavelength. The value of K/S is assumed to be proportional to the absorption coefficient within the narrow energy range of the absorption edge. The scattering coefficient S relates to the scattering of a single particle. For TiO$_2$ powders having similar crystallite size, the effect of particle size on the scattering coefficient is neglected (Table 1).

Fig. 1B shows a method to estimate band-gap values from the DRS data. TiO$_2$ crystalline undergoes indirect absorption edges under band-gap irradiation. The energy dependence of the
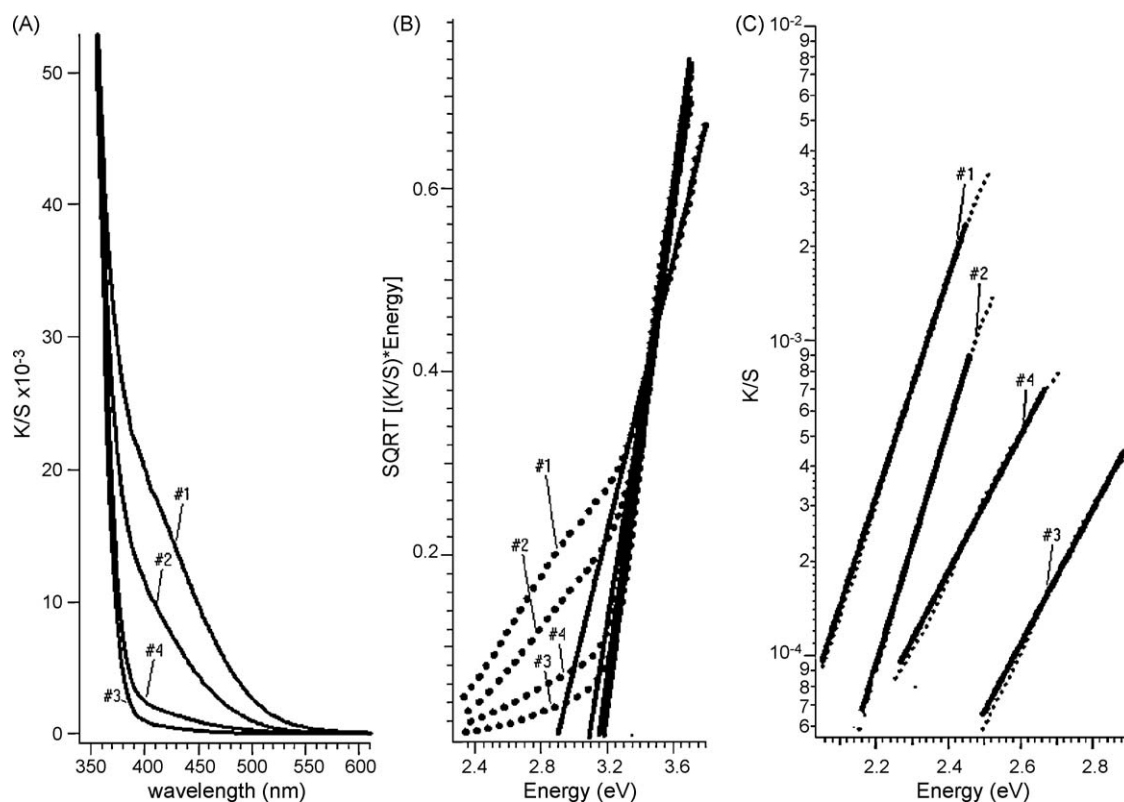
Fig. 1. Diffuse reflection spectra of doped-TiO$_2$ samples. (A) Kubelka–Munk plot of the absorbance edge. (B) Absorption plot for the indirect semiconductors transition vs. energy of the band gap. Full lines relate to the way the band gap position E_g was estimated. (C) Kubelka–Munk plot of the absorbance edge of K/S. Solid lines fit according to $K = K_0 \exp(\sigma((h\nu - E_g)/kT))$. E_g values from Fig. 1B (1) sample doped-TiO$_2$ #1; (2) sample doped-TiO$_2$ #2; (3) sample doped-TiO$_2$ #3; (4) sample doped-TiO$_2$ #4.

absorption coefficient of semiconductors near the absorption edge is given by $K \propto \left((h\nu - E_g)^n / h\nu \right)$, where E_g is the band-gap energy. The value of n is $n = 1/2$ for direct allowed transitions and $n = 2$ for indirect allowed transitions [25]. The forbidden transitions will not be considered here, because forbidden transitions by symmetry rules occur with a very low probability. The band-gap for small crystalline size semiconductor particles depend on the particle size when the Bohr exciton radius $a_B = (\varepsilon\hbar^2/m_e^*e^2)$ is comparable or higher than the particle size. Rutile has a static dielectric constant $\varepsilon \sim 100$, and an effective mass of $m^* \sim 20$ me, due to the flat conduction band and associated polaronic effects [24]. Therefore, the Bohr radius for rutile a_B is close to 2.6 Angstroms. The static dielectric constant of anatase is $\varepsilon \sim 31$, and the effective mass is $m^* \sim$ me [24]. From this, the value $a_B \sim 15$ Angstroms can be estimated. Both exciton Bohr radius of rutile and anatase are substantially smaller compared to the particle size of these powders, because the effect of the quantum confinement on the energy edge position can be neglected. The linear fit for the dependence SQRT(K/S* Energy) vs. Energy was used in the vicinity of the main TiO2 absorption as shown Fig. 1B

The intercept of the x-axis in the Fig. 1B is the value of E_g. The E_g data are shown in the Table 2.

Fig. 1C demonstrates the same spectra in a semi-logarithmic plot with x-axis being the energy scale. This presentation allows to better focus the shape of the absorption band edge. The absorption tail in Fig. 1C suggests the Urbach's energy state distribution [25]. Heavy doping of semiconductors leads to a band gap narrowing and band tailing. The band tailing implies that the band edges E_v and E_c do not have well defined cut-off energies but electronic states above E_v and below E_c with a density of states falling sharply with energies away from the band edges. This is typical for doped crystalline semiconductors and many amorphous semiconductors [25b]. An ionized donor exerts an attractive force on the conduction electrons and a repulsive force on the on the valence holes (acceptors act conversely). Since impurities are distributed randomly in the host crystal, the local interaction will be more or less strong depending on the local crowding of impurities. It should be noted that the local energy gap – the separation between the top of the valence band and the bottom of the conduction band – is maintained constant. But the density-of-states distribution, which integrates the number of states at each energy level inside the whole volume shows that there are conduction band states at relatively low potentials and valence band states in high-potential

Table 1
Specific surface area and porosity of doped-TiO$_2$ samples.

	Volume[a] (cm^3/g)	BET surface area (m^2/g)	Average pore diameter[b] (Å)
#1	0.258	94.9	31.3
#2	0.362	110.2	41.4
#3	0.427	85.6	61.1
#4	0.245	80.2	66.2

[a] BJH desorption cumulative pore volume of pores between 2 and 500 nm diameter.
[b] Average pore diameter (4 V/A by BET).

Table 2
Parameters showing the spectral characteristics of doped-TiO$_2$.

# Sample	σ/kT (eV^{-1})	E_g (eV)	BI	K_0
1	6.0 ± 0.2	2.90 ± 0.1	0.172	0.158
2	6.5 ± 0.1	3.10 ± 0.1	0.078	0.0868
3	5.7 ± 0.2	3.18 ± 0.1	0.00445	0.0025
4	4.81 ± 0.1	3.16 ± 0.1	0.0170	0.0073
TiO$_2$ P25		3.18 ± 0.07		

regions. The absorption shoulder of the doped-TiO_2 samples in the visible range can be approximated by Urbach's law: $K = K_0 \exp(\sigma((h\nu - E_g)/kT))$ [25], where K_0 is a fitting parameter, (the absorbance due to the Urbach's tail at the energy $E = E_g$), σ is a phenomenological parameter scaling the steepness of the absorption edge. In the present work the segment shown in Fig. 1C was fitted according to Urbach's law and the E_g value was determined from Fig. 1B from the fit SQRT (Energy*(K/S)) vs. Energy. The values of σ/kT and the fitting parameter K_0 for doped-TiO_2 samples are shown in Table 2. These values were found from the slope of the linear fit of the dependence of $\ln(K)$ vs. $h\nu$ in Fig. 1D.

The value of E_g for Degussa P-25 is found to be 3.18 eV and it is close to the E_g value for anatase. This is the expected because ~80% of Degussa TiO_2 P-25 consists of anatase. Table 2 shows similar values of E_g for modified TiO_2 samples and for Degussa TiO_2 P-25. This observation agrees with previous results reported for doped-TiO_2 where it was suggested that TiO_2 doped by thiourea leads to the Urbach's tail associated with the formation of states in the band-gap rather than having the effect of narrowing the band gap [18].

In addition, band integral $BI = \int(K(\nu)/\nu)d\nu$ for the absorption band in the visible was calculated for the doped-TiO_2 samples in the spectral region 2.2 eV < $h\nu$ < 2.9 eV.

The BI is the integral of the visible absorption due to the modification of TiO_2 by thiourea. The integration limits were chosen to cover the visible band and at the same time to be within the E_g of doped-TiO_2. The BI values are summarized in the Table 2. K_0 parameter is a parameter that characterizes the visible absorption due to the doping of TiO_2. The band integral BI can be used to describe the absorption in the visible region for doped-TiO_2. From now on, the band integral BI will be used. Fig. 2 shows the linear correlation between BI and K_0 values

3.2. XRD analysis of doped-TiO_2 powders

Fig. 3 presents the diffractograms of doped-TiO_2 powders. The TiO_2 crystallographic phase in Fig. 3 is anatase. Note, that if the calcination of the TiO_2 sample is made without thiourea addition, the non-doped TiO_2 has rutile 8.8% content as detected by XRD (see Fig. 3 #1b, #2b, #3b, #4b). The rutile content was determined according to formula $P_R = 1/[1 + 0.794*I_A/I_R)]$ [35], where I_A is the peak intensity of anatase (25.3°) and I_A is the peak intensity of rutile (27.5°). The doping of TiO_2 by thiourea and subsequent heating leads to products that contain no rutile. The observed anatase peaks are significantly wider in comparison with the bulk
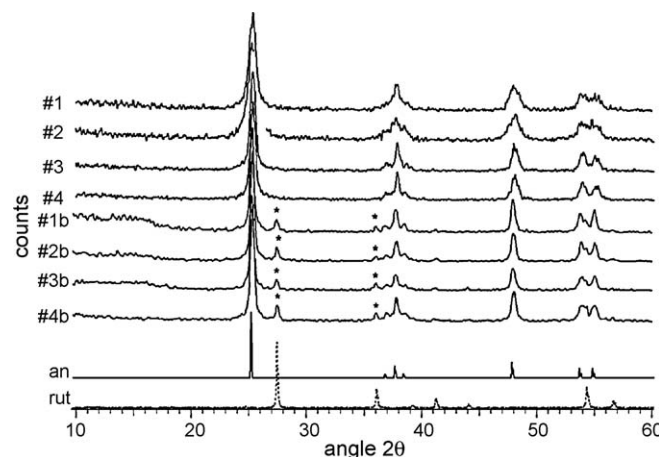
Fig. 3. XRD of TiO_2 powders. Samples of doped-TiO_2: #1; #2; #3; #4. Samples of undoped TiO_2: #1b; #2b; #3b; #4b. For the reference of bulk TiO_2 peaks of anatase (an) and rutile (rut).

TiO_2 crystal. The $FWHM$ of the TiO_2 XRD peaks of the samples are directly related to the nanocrystal size. Fig. 3 shows the $FWHM$ for the doped-TiO_2 samples. According to Debye-Sherrer formula, the size D of the crystals can be estimated by the formula: $D = (c\lambda 180/FWHM\pi\cos(\theta))$ assuming spherical particles c = 0.9; λ relates to Cu K_α 1.5418 Å [24]. The size D was estimated from the peaks at 25.3°, 37.8° and 48.1°. Error limits of D values were determined as average deviation from the D measurements of three peaks. The results are summarized below in the Table 3.

Surface Area of Doped TiO_2 Samples. The photocatalytic activity of TiO_2 is known to be a function of the surface area and increases with the BET surface area of the samples. The data about porosity and BET area of the doped-TiO_2 samples is shown in Table 1. The Ar adsorption––desorption isotherms of these samples are shown in Fig. 4. Most of the samples show a type II isotherm with hysteresis loops corresponding to capillary condensation in mesopores and a limiting uptake within the high p/p^0 region. Micropores were not detected in the studied samples. The initial part of the isotherm is attributed to monolayer-multilayer adsorption pore size distribution has been modeled using the Barrett, Joyner and Halenda (BJH) [29,31] model assuming spherical pores. The samples show a distribution of pores with sizes <10 nm (Fig. 4b)

To characterize the surface area we used two independently measured parameters: BET area (BET) and the particle diameter D. The reciprocal diameter $1/D$ is directly proportional to the ratio of the particle surface and the particle volume ν ($1/D \sim S/\nu$). BET can be obtained from the XRD-measurements for the ideal case in which the particles, besides being spherical are separated from one another. But if they are agglomerated/sintered the BET area will be smaller than values obtained by XRD. Fig. 4C shows a linear fit between BET and $1/D$ with a correlation coefficient of 0.984.

Elemental analysis was carried out to determine the content of H, N and S in the doped-TiO_2 samples. The N content was below 0.2%. This value is below the sensitivity limit of elemental analysis. The results about hydrogen and sulfur are presented in the Table 3.

Fig. 5A, B shows the correlation between the BET area of doped-TiO_2, particle size and S-content. To characterize the surface area we used two independently parameters: BET area and the particle diameter D. The reciprocal diameter $1/D$ is directly proportional to the ratio of the particle surface and the particle volume ν ($1/D \sim S/\nu$).

Qualitatively Fig. 5A, B shows that the S-content increases monotonically and not linearly, with increasing BET area. The smaller size doped-TiO_2 nanocrystals contained the higher concentration of S-atoms. Fig. 5A, B suggests that an increase in
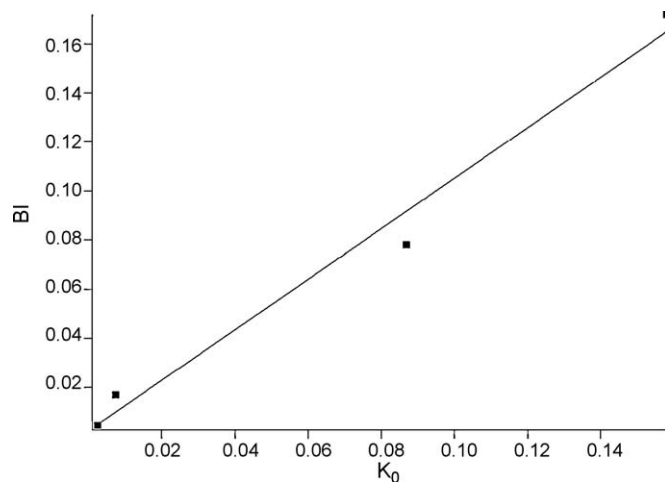
Fig. 2. Linear correlation between band integral BI and K_0 value. BI, K_0 are in arbitrary units.

Table 3
Parameters relating the doped-TiO$_2$ crystal size to the rate of C(NO$_2$)$_3^-$ formation from tetranitromethane under UV(366 nm) and visible (460 nm) light irradiation.

# Sample	Size of the particles D (nm)	H (%wt/wt%)	S (%wt/wt%)	Rate of NF formation. Excitation at 460 nm (μM/min)	Rate of NF formation. Excitation at 366 nm (μM/min)	Rate formation of I$_3^-$ Excitation at 460 nm (μM/min)	Rate formation of I$_3^-$ Excitation at 366 nm (μM/min)	Rate formation of double bond in PE Excitation at 460 nm (μM/min)
TU–TiO$_2$ #1	12.3 ± 0.2	0.86	1.15	1.6	3.8	2.4	4.9	2.0
TU–TiO$_2$ #2	9.5 ± 1.5	0.96	1.28	2.85	4.2	3.11	5.46	3.0
TU–TiO$_2$ #3	18.5 ± 1.3	0.67	0.94	1.04	9.0	1.8	16.9	0.95
TU–TiO$_2$ #4	19.1 ± 1.9	0.62	0.31	0.28	6.25	1.42	16.4	0.38
TiO$_2$ P25	25	–	–	–	2.08	–	–	–

NF: nitroform C(NO$_2$)$_3^-$.
The size of the particles was determined as average values from the Debye formula $D = (c\lambda 180/FWHM\pi\cos(\theta))$ for the three peaks at 25.3°, 37.8° and 48.1°.

the particle surface leads to an increase in S-content and could explained by the S localization on a thin surface shell around the TiO$_2$ particle. The Fig. 5B (right axis) suggests that surface concentration of S- rose up to 95 m^2/g.

We have reported recently using XPS measurements of doped-TiO$_2$ [18] that a localized surface shell of 3 nm enclosed the S and that the core of the samples consisted of almost pure TiO$_2$. The decrease of the particle size leads to the increase of the shell in the doped-TiO$_2$ relative to the core dimensions and as a consequence the S-shell becomes a more important component of the whole particle. Recently Kisch and et al., [22] reported that for TiO$_2$ doped by urea the N- was localized mainly in the core shell.

Fig. 5C, D demonstrates a correlation between spectral characteristics of the TiO$_2$ visible absorption (BI and σ/kT) and the content of S in TiO$_2$. The correlation coefficient between σ/kT and S content is 0.9827. From Fig. 5D it can be seen that correlation between visible absorption and S-atoms shows that a higher concentration of S was present in samples with a higher surface: in the sample #1 and #2, having a higher surface and a smaller diameter, the content of S was higher than in the samples # 3 and #4. The correlation coefficient between BI and S is

0.5811. At the same time, a poor correlation was observed between BI vs. S. This means that the TiO$_2$ absorption in the visible was not determined by the concentration of the S-dopant. It is possible that a low concentration of N- or C- and other structural defects, like O-vacancies (not measured in the present work) also induce absorption in the visible that can influence the BI value.

Fig. 6 correlates BI, σ/kT, the BET area of the TiO$_2$ nanoparticle and the particle diameter. The trend of a higher absorption in the sample with higher surface can be seen in samples #1 and #2. When the surface was higher, the diameter was smaller and the BI value was found to be higher than in the samples # 3 and #4. But the correlation detected for the BI vs. surface is rather poor. The correlation coefficient found was 0.4951. At the same time from Fig. 6C, D it can be seen that σ/kT and the BET area (or 1/D values) are statistically dependent. This statistical dependence show the dependence of S-content and the surface area in Fig. 5 A, B. This also applies for the correlation between σ/kT with the S-content in Fig. 5C. The physical basis for the observed statistical relations in Fig. 6 is based on the dependence of the S-content on the surface area of TiO$_2$ nanoparticles.
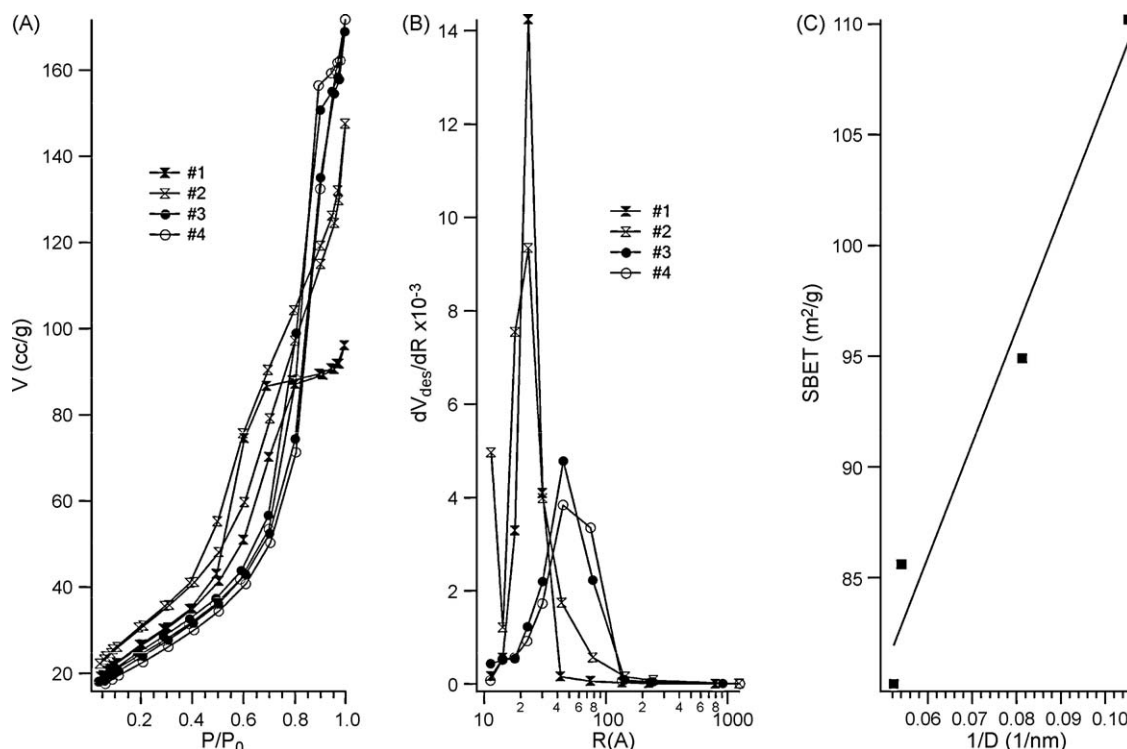

Fig. 4. (A) Isotherms of the samples: #1, #2, #3, #4. (B) Pore-size distribution for the samples: #1, #2, #3, #4. (C) Correlation between SBET and 1/D value as determined by XRD measurements.
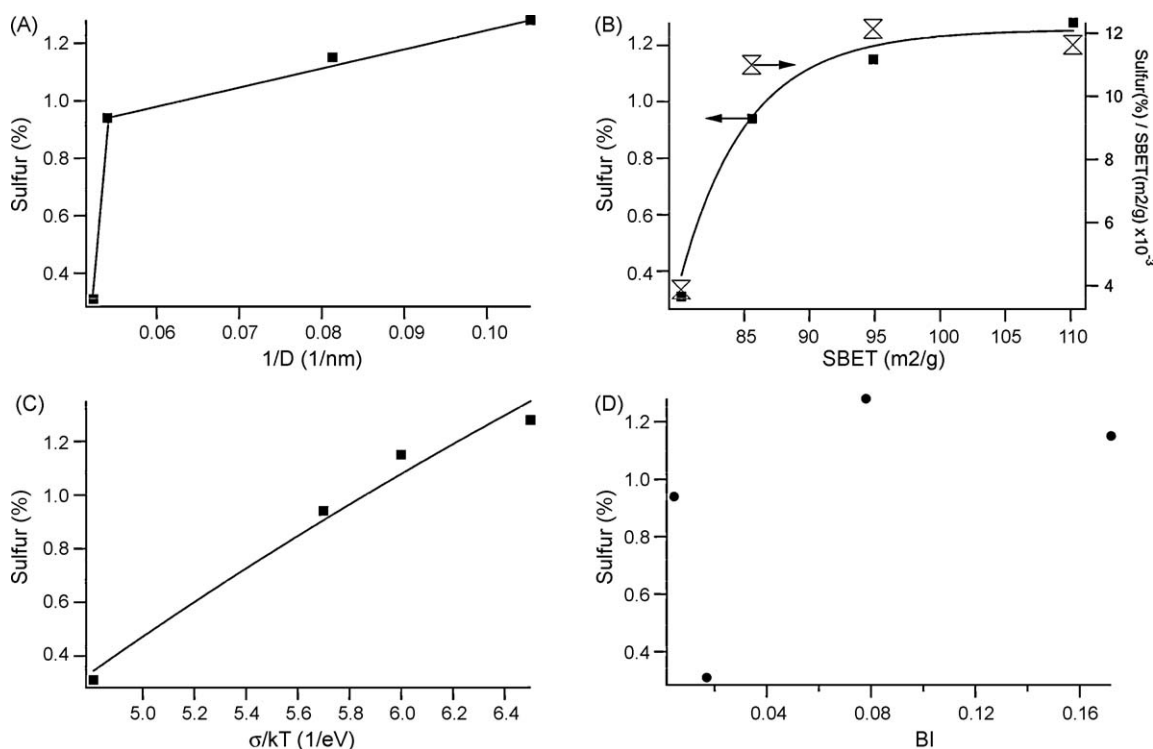
Fig. 5. Relations between the BET surface of TiO_2 particles, S-content and spectral parameters for the visible band of doped-TiO_2 particles: (A) S-content vs. the reciprocal value of the particle diameter, (B) dependence of S-content (left axis) and the S-content divided by SBET (right axis), (C) S-content vs. σ/kT and (D) S-content vs. the integral BI (BI is in arbitrary units).

The visible absorption is a product of K_0 and $\exp(\sigma((h\nu - E_g)/kT))$. A rough correlation between K_0 (or BI that correlates with K_0) is intuitively expected. The higher the concentration of doping atoms the higher is the absorbance. The correlation between σ/kT and sulfur content is less evident. The steepness of Urbach's tail

relates to the density-of-states distribution within the doped-TiO_2 integrating the number of states at each energy level inside the whole volume. The irrefutable theory to explain the observed correlation between steepness and doping atom concentration does not exist, because σ/kT is a phenomenological parameter [25,26].
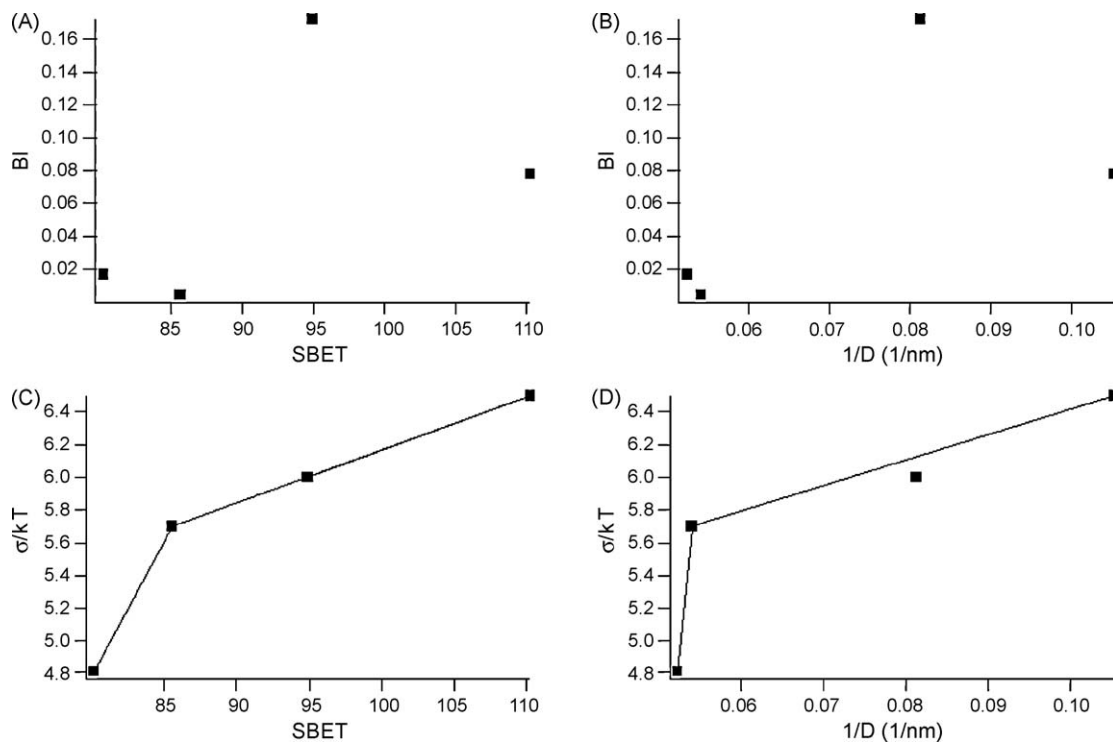

Fig. 6. Correlations between the BET and the spectral parameters of doped-TiO_2 (A) BET area and BI, (B) reciprocal value of TiO_2 particle diameter and BI. (C) BET and σ/kT, (D) reciprocal value of the TiO_2 particle diameter and σ/kT. BI is in arbitrary units. σ/kT is in units 1/eV.

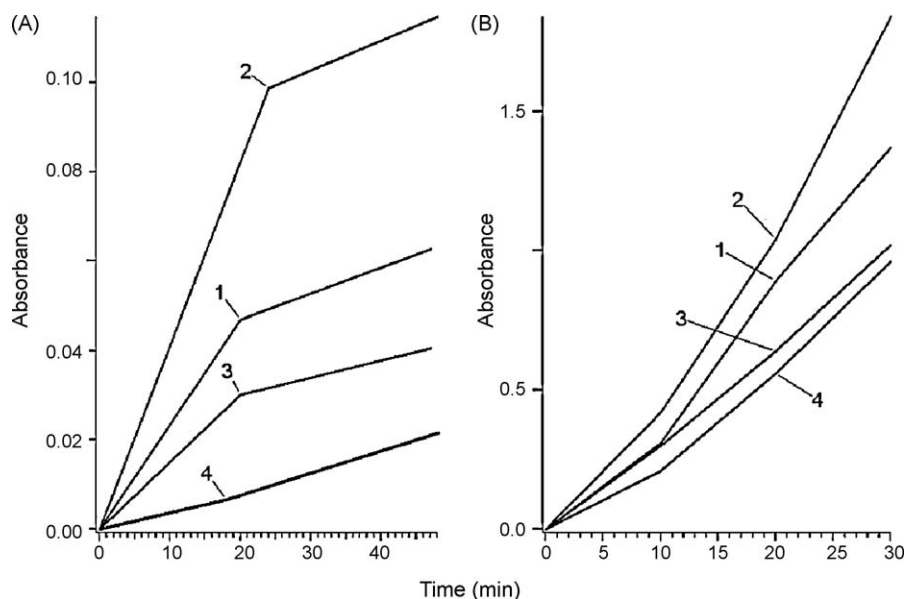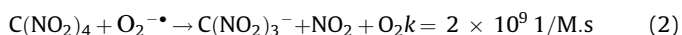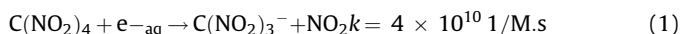**Fig. 7.** Kinetics of $C(NO_2)_3^-$ formation by the photocatalytic reduction of tetranitromethane (A) and the formation of I_3^- by the photocatalytic oxidation of I^- (B) under visible light 460 nm. The number of the kinetic curve corresponds to the number of the sample. The absorbance of $C(NO_2)_3^-$ at 350 nm (0.1 cm optical cell) and the absorbance of I_3^- at 350 nm (1 cm optical cell) are presented. In Fig. 5A, the isopropanol was added 20%, $[C(NO_2)_4] = 2.10^{-4}$ M; in Fig. 5B, [KI] = 1 M.

3.3. Photocatalytic activity

To estimate the photocatalytic activity of the doped-TiO_2 powders two test reaction were used: (1) the tetranitromethane reduction to nitroform $C(NO_2)_3^-$ and (2) the oxidation of I^- to I_3^-.

From the water radiolysis studies it is known that $C(NO_2)_3^-$ is the primary product of the reduction of tetranitromethane by solvated electrons or by ion-radical $O_2^{-\bullet}$ in reactions (1) and (2) [27]

$$C(NO_2)_4 + e_{-aq} \rightarrow C(NO_2)_3^- + NO_2 \quad k = 4 \times 10^{10} \text{ 1/M.s} \quad (1)$$

$$C(NO_2)_4 + O_2^{-\bullet} \rightarrow C(NO_2)_3^- + NO_2 + O_2 \quad k = 2 \times 10^9 \text{ 1/M.s} \quad (2)$$

Photocatalytic degradation of $C(NO_2)_4$ in the presence of TiO_2 was studied under excitation by UV light [23]. $C(NO_2)_4$ is an electron scavenger competing with O_2 [23,28]. We found that $C(NO_2)_3^-$ is produced when using doped-TiO_2 as photocatalyst under UV (366 nm) light and also under visible light (460 nm). The $C(NO_2)_3^-$ formation was detected in the presence and in the absence of isopropanol. In the absence of the isopropanol the rate of the $C(NO_2)_3^-$ formation was two times lower than when isopropanol was added into the solution. In control experiments tetranitromethane was added to doped-TiO_2 suspensions after prolonged illumination by UV or by visible light. No meaningful

amount of $C(NO_2)_3^-$ was detected. This indicates that $C(NO_2)_3^-$ was formed due to the reduction of tetranitromethane by the photogenerated e_{cb}^- from doped-TiO_2 or by $O_2^{-\bullet}$, but $C(NO_2)_3^-$ was not due to hydroperoxides generated by doped-TiO_2 under excitation by visible light as well as by UV light.

Fig. 7A shows the kinetics of $C(NO_2)_3^-$ formation due to the photocatalytic reduction of tetranitromethane mediated by doped-TiO_2 under 460 nm light. The reduction rate of tetranitromethane was estimated from the slope of the initial kinetics for the $C(NO_2)_3^-$ formation. These rates are reported in Table 3. The rate of $C(NO_2)_3^-$ formation under 366 nm light is also reported in Table 3. The samples #1 and #2 with the smaller nanocrystal sizes show the higher rate of $C(NO_2)_3^-$ formation under 460 nm light. But under 366 nm light the highest rate of $C(NO_2)_3^-$ formation was observed for the samples #3 and #4 presenting the biggest nanocrystal size.

Fig. 7B shows the oxidation of I^- anion to I_3 by 460 nm light. In Table 1 the activity towards I^- oxidation

$$h^+ + I^- \rightarrow 1/2 I_2 \quad (3)$$

$$I_2 + I^- \leftarrow \rightarrow I_3^- \quad (4)$$

was observed to parallel the degree of tetranitromethane reduction. The oxidation of I^- is due to the doped-TiO_2 photogenerated holes, proving that the h^+_{vb} holes of doped-TiO_2 have
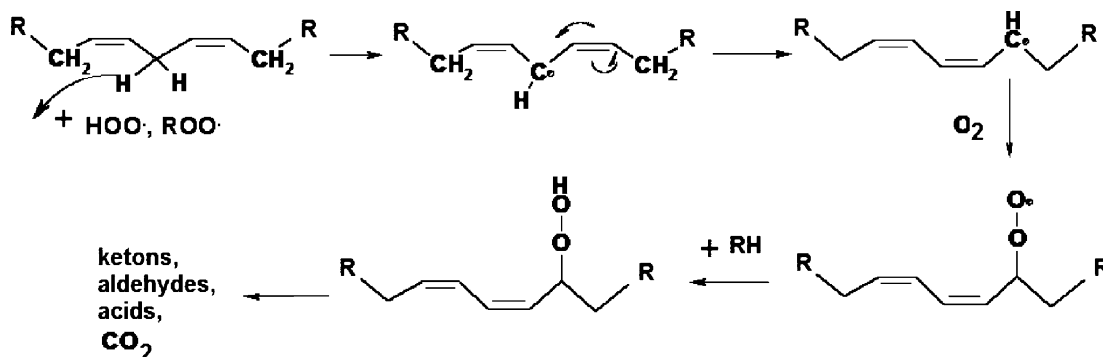
Scheme 2. Primary PE oxidation products during lipid peroxidation through $HOO^\bullet$ or $ROO^\bullet$ in the presence of O_2.

enough potential to oxidize the I^-. The rate of the I^- oxidation by different doped-TiO_2 samples correlates well with the rate of $C(NO_2)_3^-$ formation and the sample with smallest size led to the highest rate of I_3^- formation under 460 nm light excitation. The rate of I^- oxidation under UV excitation is lower for the small and more intense yellow samples (# 1, #2 samples) in comparison with the bigger TiO_2 particles (#3, #4 samples). The rates of I^- oxidation under 460 nm and 366 nm light are presented in Table 3.

The formation of PE oxidized products is considered as a test reaction for the superoxide $O_2^{-\bullet}$ radical formation [34,35]. The lipid photocatalytic oxidation by visible light is important concerning the bactericide action of doped-TiO_2. Natural lipids do not contain conjugated bonds as shown in Scheme 2. When fatty chain contains more than one double bond, lipid oxidation results in the rearrangement of double bonds to form conjugated dienes. The peak near 235 nm, so-called K band, is characteristic of conjugated double bonds present in the fatty acids [32]. The intensity of K band as it is shown in Fig. 8 can be considered as a peroxidation index [36]. Fig. 8 shows the formation of conjugated double bond under 460 nm light during the photocatalysis of PE under photocatalysis with TiO_2 sample #1. The peroxidation index with the conjugated double bond formation was followed to monitor the formation of $HOO^\bullet$ (O–$O^{\bullet-}$ radicals in net sense). Weak energy bonds like allyl 87.5 kcal/mol [33] can be oxidized by $HO_2^\bullet$ ($O_2^{-\bullet}$, $RO_2^{-\bullet}$) radicals [34], because the H–OOH bond energy is almost the same 87.45 kcal/mol [33]. The pathway for the peroxy radical formation involves the scavenging of photogenerated e_{cb}^- by O_2. The $HO_2^\bullet$ radical can react with PE as shown in Scheme 2 and this is the initiation step for PE oxidation. This leads to lipid membrane damage due to the formation toxic peroxy-radicals/peroxides. This result shows the peroxidation of the PE membrane as reported recently [29,30]. The rate of PE peroxidation under visible light is
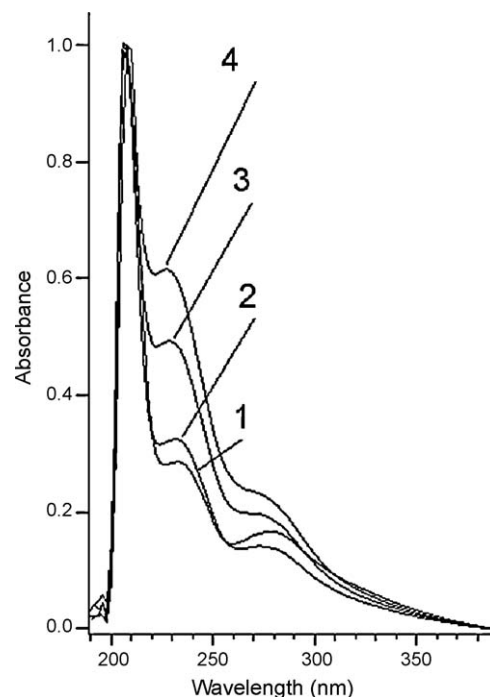

Fig. 8. Normalized absorbance spectra changes during photocatalytic peroxidation of phosphatidyl-ethanolamine (PE). Measurements were made on sample #1. Time: (1) 0 min (background of peroxidized lipid), (2) 14 min, (3) 42 min, (4) 70 min. The normalization was made for traces at λ = 210 nm. Light source 460 nm.
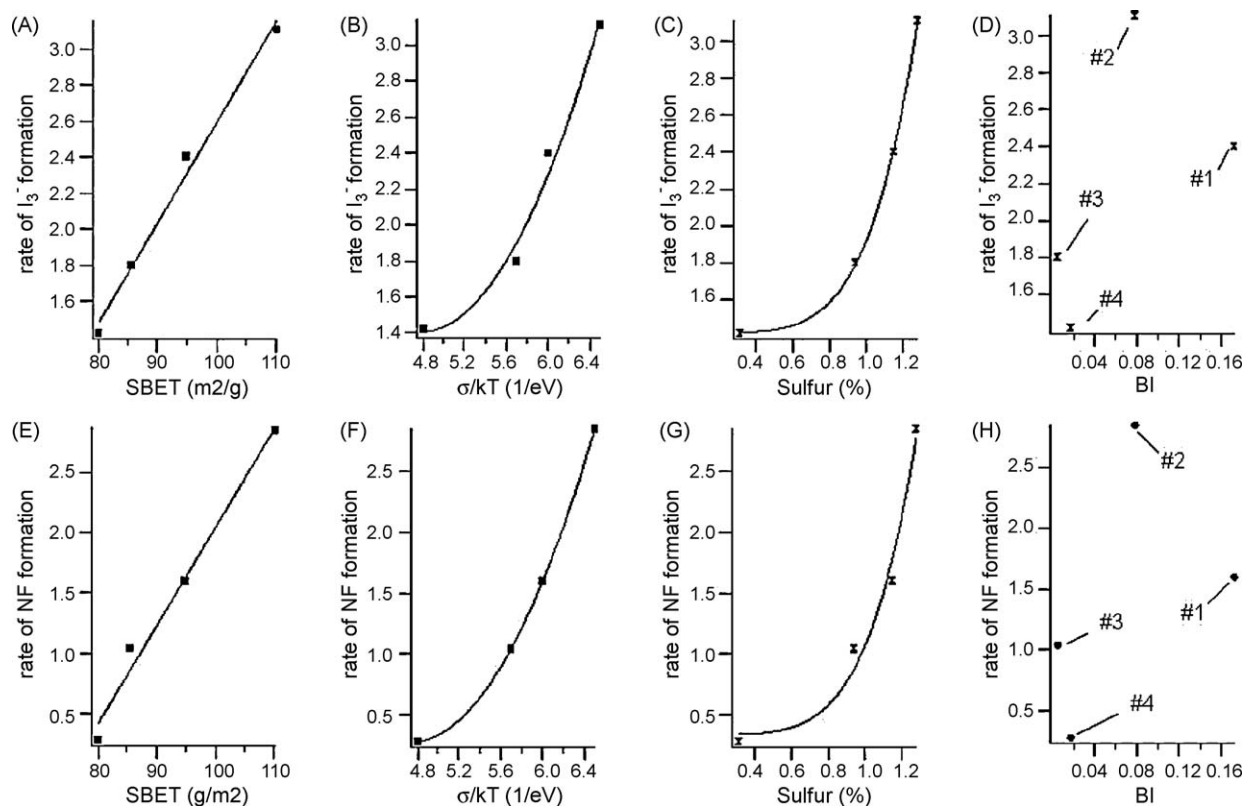

Fig. 9. Correlations between the rate of NF, I_3^- formation and BET area, σ/kT, Sulfur content, BI (under 460 nm light). The rate is presented in the units of μM/min. BI is in arbitrary units. (A) rate of I_3^- formation vs. BET, (B) rate of I_3^- formation vs. σ/kT, (C) rate of I_3^- formation vs. S-content, (D) rate of I_3^- formation vs. BI, (E) rate of NF formation vs. BET, (F) rate of NF formation vs. σ/kT. (G) rate of NF formation vs. S-content. (H) rate of NF formation vs. BI.
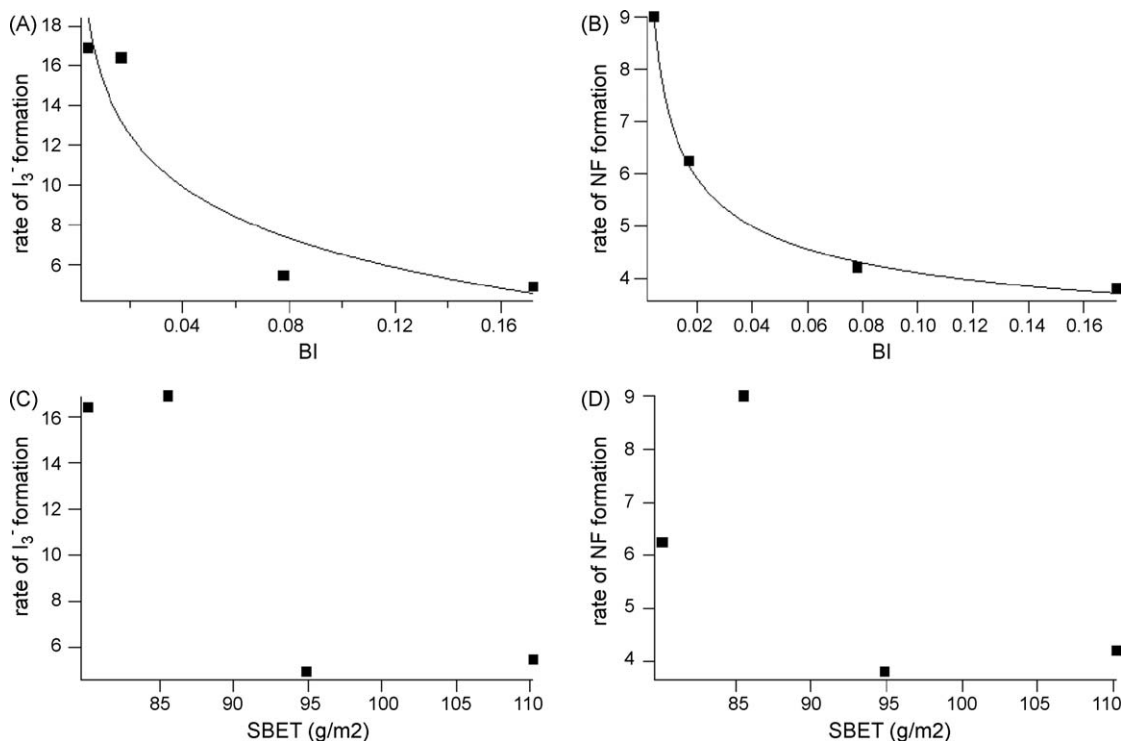
Fig. 10. Correlations between rate of NF, I_3^- formation under excitation by visible 366 nm light, BET area and *BI*. *BI* is in arbitrary units. (A) dependence of the rate of I_3^- formation vs. *BI* (B) dependence of the rate of NF formation vs. *BI* (C) a dependence of the rate of I_3^- formation vs. BET area.

reported in Table 3. The rate of PE peroxidation was observed to be higher for smaller and more intense yellow TiO_2 samples. The oxidation by the h^+_{vb} holes generated by doped-TiO_2 in dilute solutions of PE have enough potential to produce $HO^\bullet$ able to oxidize the PE. In this case it is also necessary to take into account that highly reactive $HO^\bullet$ attacks the C–H bonds in the PE with about the same rate constant and not selectively. The amount of double bonds in PE molecules involving weak C–H bonds is smaller than the total amount C–H bonds (about one or two weak C–H bonds per fatty tail of the PE molecule). The probability for $HO^\bullet$ radical to be scavenged by weak C–H bond is low and close to the value of the ratio between the weak C–H bonds and the total amount of C–H bonds in PE. The rate of PE peroxidation is close to the rate of NF formation (Table 3). As it was indicated above, the NF formation is determined by e_{cb}^- and the $O_2^{-\bullet}$ scavenging. The photochemical activity by the states from the Urbach's tail is high enough to reduce O_2 to the superoxide anion, leading to the peroxidation of lipids. This is important concerning the bactericide action of TU modified TiO_2.

Fig. 9 summarizes relations between rates of NF, I_3^- formation under visible (460 nm) and SBET, σ/kT and S-content. Fig. 9A, E shows a linear correlation between SBET and rates of NF and I_3^- formation under visible light. For the formation of I_3^- the correlation coefficient is equal to 0.9952, for the NF formation this coefficient is 0.9925. Non-linear dependences are shown in Fig. 9 B, C, F, G for the cases of NF, I_3^- formation and σ/kT and S-content. Non-linear dependences between the rates of NF, I_3^- formation and σ/kT can be considered as statistical dependences. It was shown above that BET correlates with σ/kT and BET correlates with the S-content but as non-linear functions (Fig. 5). NF and I_3^- formation correlates with BET (Fig. 9A, E) being a case of statistical dependence.

Fig. 9 D, H presents the correlations between the band integral value *BI* and the rates of NF and I_3^- formation under the visible light. The correlation coefficient for I_3^- formation is 0.5612 and for

NF formation is 0.4639. In Fig. 9 D, H the samples #1 and #2 having a more pronounced visible color present a higher rate for the reduction of $C(NO_2)_4$ and also for the oxidation of I^-. The correlations presented in Fig. 9 D, H are poor. This may be due to the fact that not all visible absorbing sites are catalytically active, or some of the absorbing visible light sites act as recombination centers for the photogenerated charge carries.

Fig. 10 shows the rates for NF formation and I^- oxidation vs. BET and vs. *BI*. Note that the rates of NF and I_3^- formation under UV (366 nm) light vs. *BI* and BET followed an opposite trend to similar dependencies when visible light was used. Fig. 10C, D reveals a decrease of the rates with increasing BET area. This suggests that the increase of the surface to volume ratio leads to an increased recombination of e^- and h^+. Fig. 10A, B also shows a decrease of the rates with an increase of the absorption in the UV. The band integral characterizes the concentration of absorbing states and their absorption cross sections. The dependences in Fig. 10A, B suggest that a decrease of the rate with increasing absorbing sites in TiO_2. These sites as well as surface states act as recombination centers for the e^- and h^+ photogenerated under light in the semiconductor band gap.

4. Conclusions

Figs. 7 and 8 show the photocatalytic activity of doped-TiO_2 under 460 nm light with quanta energy of 2.7 eV. Doping of TiO_2 leads to the narrowing of the band gap as observed in sample #1, close to an E_g value of 2.9 eV.

For all samples, the band-gap is larger than the excitation energy. This suggest that photocatalysis is due to electronic states as described by the Urbach's tail. The photogenerated e- and h^+ in the spectral region of the Urbach's tail is quite enough to reduce the $C(NO_2)_4$ to the NF, oxidize I^-, or peroxidize natural lipids. The photocatalytic activity of doped TiO_2 correlates with the BET and shows nonlinear dependence on the S-content of TiO_2. Qualitatively

the present observations can be summarized as following: the higher ratio of surface to volume the higher content of dopant atoms, more pronounced coloration, leading to a higher photocatalytic activity under visible light.

At the same time, the activity of the doped-TiO_2 under 366 nm light, followed the opposite trend relative to the excitation by visible light: samples with the larger nanocrystal diameters, showed the highest activity. Apparently this is due the decrease in the $e^- - h^+$ recombination leading to a more favorable interfacial e-transfer.

In smaller size nanocrystals a higher concentration of S-atoms was available. This lead to an increased concentration of electronic states in the band-gap. Electronic states in band gap due to S-atoms would play a double role: (a) they accelerate the charge recombination induced by the optical transition in the UV region and (b) they absorb visible light leading to the photochemical reduction of O_2 to the superoxide anion or in the oxidation of I^-.

Acknowledgments

References

[1] R. Asahi, T. Morikawa, T. Ohwaki, K. Aoki, Y. Taga, Science 293 (2005) 293.
[2] S. Sakthivel, H. Kisch, Angew. Chem. Int. Ed. Engl. 42 (2003) 4908–4911.
[3] M. Khan, M. Al-Shahry, W. Ingler, Science 297 (2002) 2243.
[4] H. Irie, Y. Watanabe, K. Hashimoto, Chem. Lett. 32 (2003) 772.
[5] K. Noworyta, J. Augustynski, J. Electrochem. Solid. -State. Lett. 7 (2004) E31.
[6] R. Asahi, T. Morikawa, T. Ohwaki, K. Aoki, Y. Taga, Jpn. J. Appl. Phys., Part 2 40 (2001) L561.
[7] T. Lindgren, J. Mwabora, E. Avendano, J. Jonsson, G. Granqvist, E. Lindquist, J. Phys. Chem. A 107 (2003) 5709.
[8] H. Irie, Y. Watanabe, K. Hashimoto, J. Phys. Chem. B 107 (2003) 5483.
[9] O. Diwald, L. Thompson, T. Zubkov, G. Goralski, D. Walck, T. Yates, J. Phys. Chem. B 108 (2004) 6004.
[10] W. Yang, L. Gao, J. Am. Ceram. Soc. 87 (2004) 1803.
[11] C. Di Valentin, G. Pacchioni, A. Selloni, A. Phys. Rev. B 70 (2004) 5116.
[12] C. Burda, Y. Lou, X. Chen, S. Samia, D. Stout, L. Gole, Nano Lett. 3 (2003) 1049.
[13] M. Mrowetz, W. Balcerski, K. Colussi, R. Hoffmann, J. Phys. Chem. B 108 (2004) 17269.
[14] T. Umebayashi, T. Yamaki, S. Tanaka, K. Asai, Chem. Lett. 32 (2003) 330.
[15] T. Umebayashi, T. Yamaki, H. Itoh, K. Asai, Appl. Phys. Lett. 81 (2002) 454.
[16] T. Umebayashi, T. Yamaki, S. Yamamoto, A. Miyashita, S. Tanaka, T. Sumita, K. Asai, J. Appl. Phys. 93 (2003) 5156.
[17] T. Ohno, T. Tsubota, K. Nishijima, Z. Miyamoto, Chem. Lett. 33 (2004) 750–751.
[18] R. Bacsa, J. Kiwi, T. Ohno, P. Albers, V. Nadtochenko, J. Phys. Chem. B 109 (2005) 5994.
[19] T. Ihara, M. Miyoshi, Y. Iriyama, O. Matsumoto, S. Sugihara, Appl. Catal. B 42 (2003) 403.
[20] N. Martyanov, S. Uma, S. Rodrigues, J. Klabunde, Chem. Commun. (2004) 2476.
[21] N. Serpone, J. Phys. Chem. B 110 (2006) 24287.
[22] H. Kisch, S. Sakthivel, M. Janczarek, D. Mitoraj, J. Phys. Chem. C 111 (2007) 1144.
[23] C. Minero, P. Piccini, P. Calza, E. Pelizzetti, New J. Chem. 20 (1996) 1159.
[24] H. Tang, K. Prasard, P.E. Smid, F. Levy, J. Appl. Phys. 75 (1994) 2042.
[25] (a) R.A. Smith, Semiconductors, 2nd. ed. Cambridge University Press, Cambridge, 1978, (b) K. Shimakawa, J. Singh, S.K. O'Leary, in: Optical Properties of Condensed Matter and Applications, John Wiley and Sons, (2006) p.47–61.
[26] L. Kovba, M. Trunov, Rentgenphase Analysis, Moscow State University, Moscow, 1976.
[27] A. Chaudry, K.D. Asmus, J. Chem. Soc. Farad. Soc. 1 (68) (1972) 1010.
[28] S. Sathivel, H. Kisch, Chem. Phys. Chem. 4 (2004) 487.
[29] J. Kiwi, V. Nadtochenko, J. Phys. Chem. B 298 (2004) 251.
[30] J. Kiwi, V. Nadtochenko, Langmuir 21 (2005) 4631.
[31] P.E. Barret, L.G. Joyner, P.H. Halenda, J. Am. Chem. Soc. 73 (1951) 373.
[32] R.B. Woodward, J. Am. Chem. Soc. 63 (1942) 1123.
[33] S.W. Benson, Thermochemical Kinetics, J. Willey & Sons, New York, 1968.
[34] I.M. Goldshtein, G. Weissmann, Biochem. Biophys. Res. Commun. 75 (3) (1977) 604.
[35] R.A. Spurr, H. Myers, Anal. Chem. 29 (1957) 760.
[36] R. Kinder, C. Ziegler, J.M. Wessels, Int. J. Radiation Biol. 71 (1997) 561.